Physics of Plasmas

RESEARCH ARTICLE | JANUARY 20 2026

Laser-induced plasma formation on free-flying liquid tin sheets

H. K. Schubert ; R. A. Meijer ; B. Liu ; D. J. Engels ; O. O. Versolato

Check for updates

Phys. Plasmas 33, 013507 (2026)
https://doi.org/10.1063/5.0307705

View Online
Export Citation

Articles You May Be Interested In

High-resolution spectroscopic imaging of atoms and nanoparticles in thin film vaporization

Appl. Phys. Lett. (December 2023)

Dependence of ion charge-energy emission from Nd:YAG-laser-produced plasma on laser intensity in the 0.4 – 40 × 10 10 W/cm^2 range

Phys. Plasmas (August 2023)

Observation of discrete concentric surface modulations on free-flying liquid tin sheets

Physics of Fluids (September 2025)

16 April 2026 10:00:48

HIDEN ANALYTICAL
Plasma Diagnostics for Fundamental and Applied Research
Mass & energy analysis of ions, neutrals and radicals
Trusted in Research for over 40 years
Find Solutions for Your Research

AIP Publishing

Physics of Plasmas ARTICLE pubs.aip.org/aip/pop

Laser-induced plasma formation on free-flying liquid tin sheets

Cite as: Phys. Plasmas 33, 013507 (2026); doi: 10.1063/5.0307705
Submitted: 17 October 2025 · Accepted: 26 December 2025 ·
Published Online: 20 January 2026

View Online Export Citation CrossMark

H. K. Schubert,[1,2] R. A. Meijer,[1,2] B. Liu,[1,2] D. J. Engels,[1,2] and O. O. Versolato[1,2,a)]

AFFILIATIONS

[1]Advanced Research Center for Nanolithography (ARCNL), Science Park 106, 1098 XG Amsterdam, The Netherlands
[2]LaserLab, Department of Physics and Astronomy, Vrije Universiteit Amsterdam, De Boelelaan 1100, 1081 HZ Amsterdam, The Netherlands

[a)]Author to whom correspondence should be addressed: versolato@arcnl.nl

ABSTRACT

We investigate the spatial and temporal dynamics of plasma formed on liquid tin sheets when irradiated with a 5 ns laser pulse at an intensity I of several 10^8 W/cm^2. From temporally integrated images of plasma emission, we deduce that there must be an intensity-specific minimum thickness at which plasma formation still occurs. Time-resolved detection of the laser light transmitted through and along the sheet reveals fast dynamics in the competition between vaporization and plasma formation. The overall dynamics are well captured in models that combine preexisting scaling laws for the time to full vaporization ($\sim I^{-1}$) and the time to plasma onset ($\sim I^{-2}$). These findings are particularly relevant for target preparation and metrology in plasma light sources utilizing tin targets to produce extreme ultraviolet light for nanolithography applications, including metrology.

© 2026 Author(s). All article content, except where otherwise noted, is licensed under a Creative Commons Attribution (CC BY) license (https://creativecommons.org/licenses/by/4.0/). https://doi.org/10.1063/5.0307705

16 April 2026 10:00:48

I. INTRODUCTION

Laser-induced plasma plays a key role in applications such as thin-film deposition and spectroscopic analysis. In pulsed laser deposition (PLD),[1,2] high-energy laser pulses ablate a target material, generating a plasma plume that enables precise thin-film growth, critical for electronic and optical devices. Laser-induced breakdown spectroscopy (LIBS) provides real-time elemental analysis in fields ranging from geochemistry and space exploration to industrial quality control.[3] Recent advances in plasma monitoring, dual pulse laser techniques, and artificial-intelligence-driven diagnostics continue to refine the capabilities of laser-induced plasma technologies.[4,5] This study investigates the plasma-formation threshold and spatial plasma dynamics on liquid tin sheets under nanosecond laser irradiation, contributing to the development of extreme ultraviolet (EUV) light sources for nanolithography. In these sources, mass-limited tin droplets serve as targets in a multipulse laser scheme.[6–9] First, a nanosecond-duration prepulse (PP) accelerates the droplet to a center-of-mass speed (U) in the order of 100 m/s. It simultaneously initiates a radial expansion of the droplet, forming a thin sheet with a radius of order 100 μm that improves the overall coupling with the following main pulse, which generates the EUV-emitting plasma.

In this work, we focus on the interaction between a vaporization laser pulse (VP) and liquid tin sheets for laser intensities $I_{VP} > 1 \times 10^8$ Wcm^{-2}. Previous studies have examined laser-induced vaporization of liquid tin sheets at lower laser intensities ($\sim 5 \times 10^7$ W/cm^2), below the plasma formation threshold. Such controlled laser-induced vaporization of liquid tin sheets has been shown to facilitate the formation of a low-density vapor while simultaneously revealing key features of the evolving sheet, such as a characteristic center mass and a bounding rim.[10–12] In this regime, the evaporation process is dominated by gradual Hertz–Knudsen evaporation,[10–12] and the resulting low-density vapor primarily consists of atomic tin at approximately 3000 K, accompanied by nanoparticles.[10] With increasing laser intensity, plasma formation first emerges on the thicker regions of the sheet, causing a sharp increase in vapor temperature to as high as 8000 K.[13] Here, plasma formation is hypothesized to suppress nanoparticle formation, resulting in a vapor composed entirely of free atoms.[13] In addition, previous work on liquid tin microdroplets has revealed an inverse square dependence of the plasma onset time on laser intensity, when irradiated with nanosecond laser pulses with intensities ranging from 4×10^7 to 4×10^8 W/cm^2.[14] This behavior has been attributed to one-dimensional heat diffusion during the irradiation process relevant for a bulk medium. No study has specifically investigated the laser-induced plasma-onset time and the spatiotemporal dynamics of plasma formation using thin sheets, where vaporization and plasma

© Author(s) 2026

phases may coexist. This is especially interesting given that (liquid) thin sheets serve as targets for laser-produced plasma that generates EUV light in state-of-the-art nanolithography. Experimental studies on vapor-plasma phase transitions are essential for refining laser-droplet interaction models, with direct relevance to EUV source development in droplet shaping, debris mitigation, and metrology.

We investigate the spatial and temporal dynamics of plasma formation on liquid tin sheets by irradiating them during the droplet deformation process with a 5 ns laser pulse at intensities near the threshold of plasma formation. We employ an imaging system (combining bright field with shadowgraphy) to detect plasma emission and photodiodes to measure laser pulse transmission. From the imaging, we observe that the extent of the sheet plasma does not continuously follow the sheet boundary throughout the deformation process, but instead reflects an intensity-specific thickness at which plasma formation occurs before vaporization (see Sec. III A). Photodiode traces reveal that the laser transmission exhibits a reproducible inflection point in time, depending on laser pulse intensity and droplet deformation time (see Sec. III B). We attribute the observed inflection point to the moment when the vapor and plasma phases intersect, at a threshold thickness that is a function of laser intensity. Finally, we produce a vapor-plasma phase map using all experimental inflection time and thickness data and show agreement with a model that combines preexisting vaporization and plasma onset scaling laws.

II. EXPERIMENTAL METHODS

Our experimental setup, previously described in detail,[11,12] employs a droplet generator to produce a kHz stream of (270 °C) liquid tin microdroplets traveling at ∼10 m/s in a vacuum environment at a base pressure of 10^{-7} mbar. The microdroplets traverse a HeNe laser light sheet. Scattered HeNe light is detected via a photomultiplier tube. This signal is next downsampled to 10 Hz and triggers the experiment and synchronizes all lasers. Figures 1(a)–1(c) illustrates the laser pulse scheme. We utilize a pre-pulse (PP, $\lambda = 1064$ nm, circularly polarized) to generate plasma upon interaction with the initial microdroplet, inducing an impulsive acceleration of approximately 10^{10} m/s^2. This rapid acceleration launches the droplet to velocities of ∼100 m/s, initiating a strong radial expansion and leading to the formation of a thin sheet.[15] The initial radial expansion velocity ($\dot{R}_0$, measured over the first three frames where R_0 stands for droplet radius) decreases over the capillary timescale $\tau_c = \sqrt{\rho D_0^3/6\sigma}$ due to surface tension driven sheet contraction, while the propulsion velocity (U) remains constant.[16–18] Here, $\rho = 7000$ kg/m^3 and $\sigma = 0.55$ N/m represent the density and surface tension of the liquid tin, respectively, while D_0 is the initial droplet diameter. The vaporization pulse (VP, $\lambda = 1064$ nm, circularly polarized), as shown in Fig. 1(a), is a 5 ns Nd:YAG pulse imaged to a top-hat spot with a FWHM of 822 μm with an intensity of the order 10^8 W/cm^2, which vaporizes the sheet and initiates plasma formation. We tune I_{VP} by means of a half-wave plate, followed by a polarizing beam splitter cube, positioned in front of the chamber. Spatially, the VP beam profile exhibits a standard deviation variation of approximately 6% across its cross-sectional area. Temporally, the beam intensity varies with a standard deviation of less than 3% over the pulse duration t_{VP}. The VP is larger than the sheets that we probe at any time during droplet deformation, allowing us to analyze the VP transmission signal using photodiodes (DET025AL/M) installed at the entrance and exit of our measurement setup. For spectroscopic imaging, we use a dye-based illumination source (5 ns, 560 nm, temporally and spatially incoherent) in combination with CCD cameras (Manta G-145B NIR PoE) and long-distance microscopes, providing a spatial resolution of 5 μm in front and back views [Fig. 1(b)]. Both cameras are equipped with a 560 nm narrow-band filter. The illumination is fixed at 100 ns after the VP [Fig. 1(c)] to allow some separation between the imaging of the VP-induced plasma and the liquid remnant while limiting hydrodynamic evolution (including fragmentation). Both the laser-induced plasma emission and the liquid tin remnants are captured because the camera exposure time is significantly longer (on the order of μs) than the 100 ns separation between VP and SP. The VP is scanned in $\Delta t = 60$ ns steps with respect to the PP. At each delay step, 20 frames are captured using stroboscopic

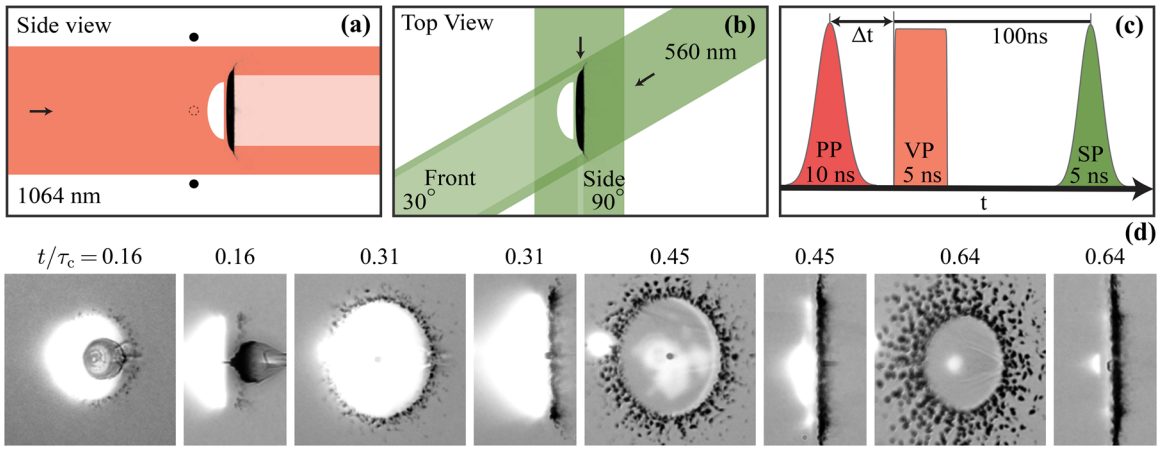

FIG. 1. (a)–(c) Schematic of the experimental laser pulse scheme with irradiation geometries and timings shown. (a) Side-view schematic of the vaporization pulse (VP) irradiating the liquid tin sheet. (b) Top-view schematic of the illumination setup. (c) Timing of the shadowgraphy pulse (SP). The VP is scanned over time Δt, with the SP following the VP after 100 ns. (d) Series of shadowgraphs showing alternating views of sheet residue and laser-induced plasma emission in front-view (left) and side-view (right) at various times t/τ_c during droplet deformation following VP irradiation with $I_{VP} = 4.7 \times 10^8$ Wcm^{-2}. The small bright spot on the left side of the front-view image, especially visible at $t/\tau_c = 0.45$, originates from PP plasma emission.

16 April 2026 10:00:48

© Author(s) 2026

imaging. We attribute visible light emission as the primary indicator for plasma formation, consistent with prior studies,[14] and refer to it in the following simply as *plasma*.

To quantify the radial extent of the sheet plasma, we define a threshold to binarize the image accordingly. A plasma pixel is defined as a pixel within the top percentile (upper 10%–30% depending on the experimental conditions) of all pixel values between the maximum pixel value and the mean of the background. The threshold is individually set for each I_{VP} scan to best capture the sheet plasma extent during the expansion phase, which closely follows the evolution of the liquid sheet. In addition, we apply image-processing techniques to track the radius of sheet plasma and not the rim plasma (see Measurements). The shadowgraphs, shown alternately in front and side-views [Fig. 1(d)], capture the sheet and its plasma at various stages of droplet deformation. The front-view shadowgraphs highlight that minor (the aforementioned 6% variation) spatial imperfections in the beam profile translate to visible differences in plasma light emission, highlighting the non-linear behavior at plasma threshold. In contrast, side-view shadowgraphs are less sensitive to beam profile imperfections as a result of their line-of-sight integration over a larger portion of the beam. For radial quantification, we exclusively use side-view shadowgraphs, which offer longer plasma columns and higher brightness compared to the front view; the corresponding results are discussed in Sec. III A. Furthermore, we measure VP transmission using photodiodes, which provide a radially integrated signal that is largely insensitive to minor beam inhomogeneities; these results are presented in Sec. III B.

III. MEASUREMENTS

A. Imaging of plasma emission

From the shadowgraphs in Fig. 1(d), we observe that the laser-induced sheet does not always form over the full sheet during the target deformation process. We note that the sheet expansion has been studied in detail previously (see, e.g., Refs. 19, 17, and 20), and in the current work, we solely focus on the plasma produced from the sheets. For the given I_{VP}, the radial extent of the sheet plasma initially follows the sheet's expansion, as seen for $t/\tau_c \leq 0.31$. In this early phase, plasma spans the entire sheet, which we define as the *bulk* regime. Here, the sheet is sufficiently thick that irradiation by the VP leads to plasma formation all over the sheet, consistent with observations in previous laser-droplet interaction studies.[14] At later times ($t/\tau_c = 0.64$), plasma formation becomes confined to the sheets' thicker center and rim of the sheets, whereas the remainder of the sheet vaporizes without producing visible laser-produced plasma. We refer to this condition as the *thin film* regime, as studied in Refs. 11 and 12. Between these two regimes, there is the *intermediate* regime, illustrated by the shadowgraph at $t/\tau_c = 0.45$ in Fig. 1(d). In this regime, plasma emission is partially observed around the sheet center and the rim of the sheet, whereas the outer, thinner sheet regions atomize without contributing to plasma formation.

It is important to note that the shadowgraphy observations of the sheet plasma are time-integrated over the VP duration (5 ns), as the camera exposure time is significantly longer ($\sim\mu$s). The shadowgraphs therefore show only the integrated result of the emission. At any stage of the droplet deformation process, the sheet exhibits a radially decreasing thickness profile and progressively thins over time.[20] We observe that the sheet-plasma radius initially follows the sheet expansion (*bulk* regime) but at some point decreases rapidly (*intermediate* regime). This suggests the existence of an intensity-dependent minimum sheet thickness required for plasma formation, as we argue in the following.

From previous studies, the time required for vaporization of a *thin film* is known to scale as

$$t_{VP} = \frac{h(r)}{A \times I_{VP}}, \tag{1}$$

where $h(r)$ denotes the local sheet thickness, $A = 1.0(3) \times 10^{-7}\,\mathrm{ms^{-1}/Wcm^{-2}}$ is a proportionality constant obtained by fitting, and I_{VP} is the laser intensity.[11] Physically, A reflects the balance between the laser energy deposited and the energy required for vaporization and may be estimated by evaluating the energy required to vaporize a unit volume of tin $\rho H/M$, where ρ is the density, H is the latent heat, and M is the molar mass. Assuming a 20% absorption coefficient a, Schubert *et al.*[11] estimated the prefactor $1.2 \times 10^{-7}\,\mathrm{ms^{-1}/Wcm^{-2}}$ (explicitly from $A \approx aM/\rho H$) close to the original fit result.[11] Figure 2 illustrates how the time to full (local) vaporization t_{VP} scales with intensity I_{VP} with a prefactor set by the initial (local) thickness.

In contrast, the onset of plasma formation in a *bulk* medium is known to follow:

$$t_{on} = B \times I_{VP}^{-2}, \tag{2}$$

where $B = 3.4(4) \times 10^{8}\,\mathrm{sW^2/cm^4}$ is a proportionality constant obtained from fitting.[14] Physically, B represents 1D laser heat diffusion following energy deposition within the thermal absorption layer and may be estimated (see Ref. 14 for details) from evaluating the energy required to reach a pulse length dependent threshold fluence $F_t = \rho H\sqrt{\kappa\tau}/M$, where κ is the thermal diffusivity and τ the laser pulse length. Assuming a 16% absorption coefficient, Meijer *et al.*[14] estimated a prefactor $B = 4.4 \times 10^{8}\,\mathrm{sW^2/cm^4}$ (explicitly from the approximate relation $B \approx (\rho H\sqrt{\kappa}/aM)^2$) in reasonable agreement with the original fit result.[14] Figure 2 illustrates how the time to plasma

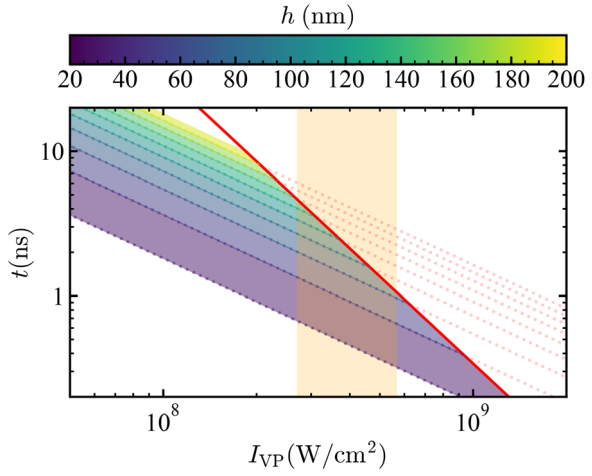

FIG. 2. Vaporization time $t_{VP} \propto I_{VP}^{-1}$ [Eq. (1)], for different initial local thicknesses (indicated by the color bar). The plasma onset time $t_{on} \propto I_{VP}^{-2}$ [Eq. (2)] is shown in red. The shaded yellow region highlights the experimental measurement range.

16 April 2026 10:00:48

© Author(s) 2026

onset t_{on} scales with intensity I_{VP} with a prefactor that is independent of the local thickness.

In the *intermediate* regime, both vaporization and plasma coexist, depending on the local thickness [cf. Fig. 1(d) at $t/\tau_c = 0.45$]. For a given I_{VP}, both models intersect when $t_{VP} = t_{on}$ at a thickness

$$h^* = \frac{A \times B}{I_{VP}}, \tag{3}$$

or, as approximated in terms of the underlying material constants $h^* \approx (\rho H \kappa / aM)/I_{VP}$. Beyond this thickness, gradual vaporization transitions into plasma formation. However, we emphasize that this intersection point [Eq. (3)] serves only as an upper limit given that, as the sheet thins, the surface temperature will rise faster than in the bulk case and t_{on} will shift to earlier times. Consequently, Eq. (3) should also be interpreted as an upper bound, and the intensity scaling exponent α of t_{on} will deviate from the value $\alpha = -2$ (ranging $-2 < \alpha < -1$ with -1 yielding the thin sheet limit).

Returning to the shadowgraphs in Fig. 1(d), we find two further distinct features that exhibit plasma formation. The first feature is the rim (and associated ligaments and ligament-fragments) that bounds the sheet.[20] Hydrodynamic arguments predict that its diameter is in the order of 1 μm.[20] The second feature is the center mass,[21] also with a thickness of a few μm. These regions are significantly thicker than the sheet and well exceed the threshold h^*. As a side note, we observe that the fragments ejected by the rim ligaments appear larger at later times (100 ns) due to the combined effects of fragment size increasing with time[21] and partial vaporization leading to an dense, partially opaque expanded vapor surrounding the fragments. From hereon, we focus our studies on the central sheet that presents a window on the intermediate regime and track the lateral plasma size (cf. Sec. II) over time.

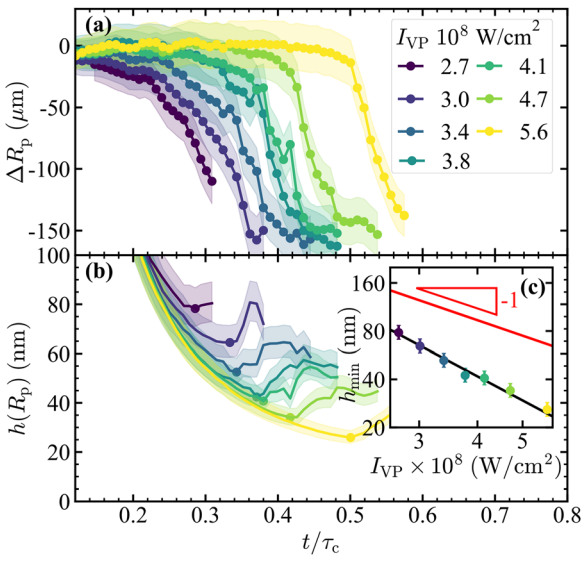

FIG. 3. (a) Difference plasma radius ΔR_p for various I_{VP}. (b) Sheet thickness at the plasma emission radius R_p during expansion for various I_{VP}. (c) Minimum sheet thickness identified in (b) as a function of I_{VP}; the red line presents the threshold thickness h^* [see Eq. (3)].

In Fig. 3(a), we plot $\Delta R_p = R_p - R_{exp}$, where ΔR_p is the difference between the lateral extent of the plasma R_p and the radius of the liquid sheet R_{exp}. We observe that the VP-induced sheet plasma radius initially closely follows the sheet expansion trajectory (that is, $\Delta R_p \approx 0$) before deviating at an intensity-dependent time. For a higher I_{VP}, the contraction of ΔR_p occurs later and more abruptly. In Fig. 3(b), we present the sheet thickness at R_p using the semi-empirical model by Liu *et al.*,[20] developed for laser-shaped tin targets. This model was inspired by the self-similar solution by Wang and Bourouiba[19] for the case of water-pillar impact. Using this model of Liu *et al.*[20] to calculate the sheet thickness leads to the observation that, for each I_{VP}, there is a minimum thickness below which the sheet plasma is no longer observed. In both panels of Figs. 3(a) and 3(b), the error bars on ΔR_p and $h(R_p)$ represent uncertainties from radial sheet plasma tracking ($\pm 10\%$) in (a) and an additional uncertainty from thickness estimation due to the input parameter $\dot{R}_0$ ($\pm 5\%$) in (b), see Ref. 20. In Fig. 3(c), we plot the minimum thickness h_{min} at which plasma is observed as a function of I_{VP} and find that it decreases with increasing I_{VP} in line with expectation cf. Eq. (3).

The h_{min} in Fig. 3(c) extracted from (b) follows a somewhat steeper slope than predicted with Eq. (3) for h^* and lies systematically below it.

Overall, we observe reasonable agreement between the experiment and our model without performing any fit. This agreement is in fact surprising given the experimental limitations and the strongly simplified model, even more so given the fact that R_p is here determined from images that necessarily integrate the plasma emission over the full VP duration and thus is blind to any dynamics on the VP timescale.

B. Time-resolved laser transmission

To gain a deeper insight, we next examine the temporal dynamics of the interaction between the VP and the liquid tin sheets using photodiode (PD) measurements of the VP beam that is transmitted past the tin sheet (cf. Sec. II). To process the transmission PD data, we first apply an offset correction to all traces, then average the traces for each delay t/τ_c, and finally normalize all data. For the normalization we use, for each measurement independently, an early-time reference PD trace measured prior to the PP–droplet interaction. Prior to this interaction, there is only negligible ($\approx 0.1\%$) geometrical overlap between the VP and the unexpanded droplet.

Figure 4 shows a heatmap of the measured VP transmission (z-axis) as a function of the droplet deformation time t/τ_c (x-axis) and VP duration t_{VP} (y-axis) for $I_{VP} = 4.7 \times 10^8$ Wcm^{-2}. For better visibility, the color scale is limited to the range of 65%–100%. This range is appropriate because the VP beam (diameter 822 μm) always partially bypasses the expanding sheet, resulting in an offset in the transmission dynamics. The PD signal at $t/\tau_c = 0$, when the VP impacts the droplet simultaneously with the PP, shows a noticeable dip compared to one earlier and one later time step, highlighting the effect from PP-induced plasma formation on the droplet, which causes absorption of the VP (via inverse Bremsstrahlung). Next, for $0 < t/\tau_c < 0.1$, the PD signal gradually decreases in amplitude but remains approximately constant over the duration of the VP. We attribute the gradual decrease in VP transmission (at any t_{VP}) with t/τ_c to the liquid tin sheet's expansion: as the sheet expands, it spans a larger

16 April 2026 10:00:48

© Author(s) 2026

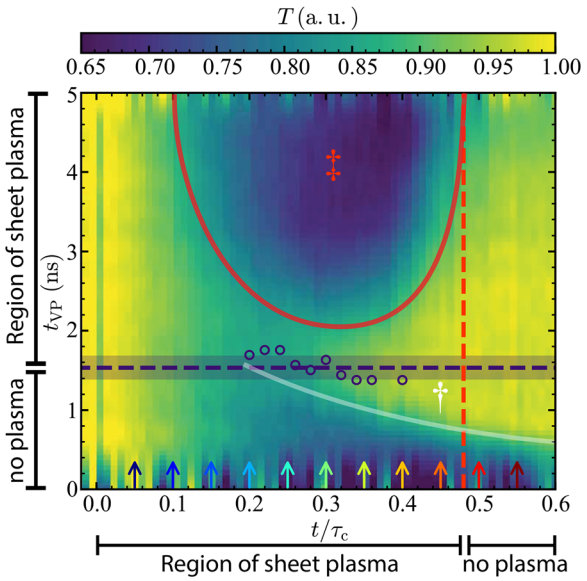

FIG. 4. Heatmap of the transmission T (color axis) during the 5-ns long VP irradiation, for a fixed intensity ($I_{VP} = 4.7 \times 10^8$ W/cm^2), plotted over normalized droplet deformation time t/τ_c (x-axis) and VP duration t_{VP} (y-axis). The horizontal dashed line marks the onset of plasma formation based on Eq. (2) and is accompanied by a shaded band indicating the ± 150 ps systematic uncertainty in t. The hollow markers denote the transmission maxima for selected t/τ_c. The red dashed vertical line marks the last time step at which plasma is observed via shadowgraphy. The region above white line † corresponds to increased transmission due to vaporization of the thinner outer regions of the sheet. The region outlined by the red solid line ‡ highlights a sharp drop in transmission, attributed to plasma formation. Colored arrows along the bottom denote the time line-outs used in Fig. 5. Regions labeled "Region of sheet plasma" and "No plasma" summarize plasma presence as inferred from photodiode data (vertical axis) and shadowgraphy (horizontal axis, cf. Fig. 1), respectively.

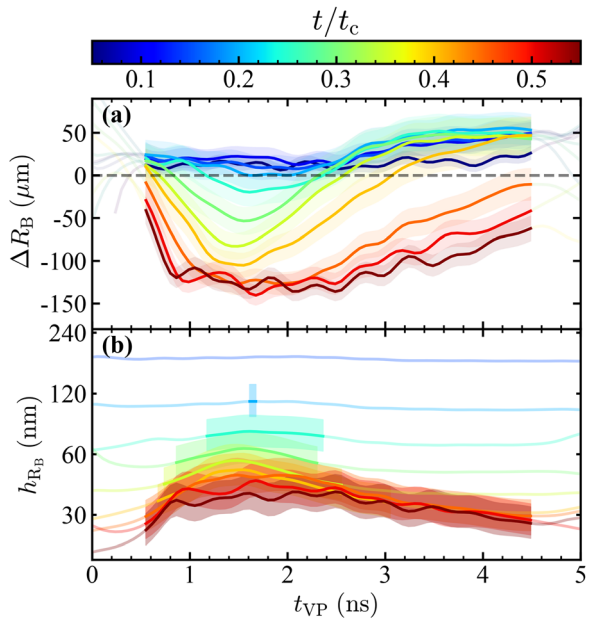

FIG. 5. (a) Difference blocking radius ΔR_B as a function of t_{VP} for selected time steps t/τ_c for $I_{VP} = 4.7 \times 10^8$ Wcm^{-2}. (b) Sheet thickness at R_B as a function of t_{VP}. Only $R_B < R_{sheet}$ can yield physically relevant values for the thickness; regions $R_B > R_{sheet}$ are faded.

cross-sectional area within the VP beam, thereby reducing the transmitted signal.

Focusing next on $t_{VP} = 0.5$, the gradual decrease with increasing t/τ_c is fully explained by this increasing geometrical liquid-sheet cross section. At larger t_{VP}, the same decrease in transmission remains visible up to the white line that highlights (as visual guide) the shrinking of the geometrical liquid-sheet cross section due to vaporization. This white line moves to a higher t_{VP} for decreasing t/τ_c as for thicker sheets (earlier times t/τ_c) shrinkage starts later in the VP given that more vaporization is required. We plot the white line up to $t_{VP} \approx 1.5$ ns (indicated by the transparent band that takes into account the timing uncertainty inherent to the measurements), where the bulk plasma threshold is reached; cf. Eq. (2). We attribute the drop in transmission for a larger $t_{VP} > 1.5$ ns (specifically in the region enclosed by the red solid line, again as a visual guide) to plasma formation, decreasing transmission. We mark the moment of transmission drop in the photodiode (PD) signal at intermediate values t/τ_c (open purple markers). We note that the observed transmission drop due to plasma formation could result from inverse Bremsstrahlung absorption of VP, but also in part be due to lensing by gradients in the plasma. In addition to geometric blockage by plasma formation, dense fragment clouds could contribute to attenuation, particularly at later times $t/\tau_c > 0.5$, when the number of droplets within the vaporization pulse (VP) beam, as well as the diameter and size of the fragment rim, increases with t/τ_c.[21] The plasma formation region enclosed by the red solid line is bounded on the right by $t/\tau_c \approx 0.45$ at which point the entire sheet is too thin to support plasma formation. The region is limited on the left by the hypothesized (not shown) merging of the red and white vaporization lines; however, at this point, the signal-to-noise ratio no longer supports identifying a maximum in transmission.

Importantly, we only observe a distinct inflection point in the photodiode (PD) signal when plasma light emission is also visible at the sheet position in the shadowgraph images.

We therefore label the regions "Region of sheet plasma" and "No plasma" to indicate the inferred presence of plasma, based on photodiode data (vertical axis) and shadowgraphy observations (horizontal axis; see Fig. 1).

To make a quantitative connection with the shadowgraph frames (and the data in Fig. 3), we extract a *blocking* radius R_B from a conversion of the photodiode transmission signal. This heuristic conversion is based on the simple Ansatz of a circular top-hat beam and a circular blocking element of radius R_B that geometrically blocks the light from reaching the PD. We use the linear relation between the normalized PD signal trace, which yields the beam transmission (T), and the beam area transmitted A_T, which is given by $A_T = T \times A_{beam}$. The corresponding blocked beam area A_B is then $A_B = A_{beam} - A_T$. From this, we determine the blocking radius R_B as

$$R_B = \sqrt{\frac{A_B}{\pi}} = \sqrt{R_{beam}^2 \times (1 - T)}, \tag{4}$$

and, in line with Sec. III A, we focus on the difference radius $\Delta R_B = R_B - R_{exp}$. Figure 5(a) shows ΔR_B as a function of t_{VP} for

16 April 2026 10:00:48

© Author(s) 2026

selected droplet deformation times t/τ_c [cf. vertical arrows in Fig. 4(a)]. The shaded region indicates the uncertainty in R_B, resulting from an estimated uncertainty 5% in determining R_{beam}. We find that R_B follows the shadowgraph-inferred sheet radius during early times of t_{VP} aside from overestimating the sheet radius by up to 15% at the early times (< 1 ns), which we attribute to the exclusion of fine structures and ligaments in the shadowgraph analysis (where we track the rim), features that contribute to geometrical blocking and, thus, to R_B. The interpretation of R_B should be made with care in the following given that the ansatz of a single circular blocking element represents a strong simplification. To avoid bandwidth limitations and other electronic artifacts, our quantitative PD analysis is restricted to the interval between 0.5 and 4.5 ns. Soon after the onset of VP, ΔR_B shrinks to an inflection point, after which it increases again. This dynamic becomes more pronounced for later time t/τ_c. We observe that ΔR_B levels off at positive values at the end of the VP, indicating $R_B > R_{sheet}$. The observation of the PD data in terms of ΔR_B makes clear that the time-integrated plasma emission shadowgraphs hide a rich fast dynamic [compare Figs. 3(a) and 5(a)]: gradual vaporization reduces ΔR_B until the plasma sparks on thicker regions underlying the increase in ΔR_B. In our interpretation of a blocking radius, the fast dynamics of the increase in ΔR_B corresponds to an expansion speed of several tens to 100 μm/ns. Such high speeds have been predicted by simulations[22] on ionization waves propagating through subcritical tin vapor. Laser-induced ionization waves in gases, such as air and argon, have been experimentally observed to propagate at similarly high supersonic speeds (10–30 μm/ns).[23]

We attribute the observed inflection points in Fig. 5(a) [cf. open circles in Fig. 4] to the moments when the vapor and plasma phases intersect at a threshold thickness h^*. Given that the sheet thins over time t/τ_c,[20] the threshold thickness (for a given laser intensity) moves radially inward on the sheet with increasing time t/τ_c, and thus, h^* is found at ever larger negative values of ΔR_B (that is, it is found ever closer to the center of the sheet).

In Fig. 5(b), we next present the thickness calculated at the blocking radius as a function of t_{VP} for the same selected droplet deformation times t/τ_c. The shaded region indicates the uncertainty in h_{R_B}, arising from an estimated 10% uncertainty in the radial expansion speed $\dot{R}_0$ and a 5% uncertainty in R_B. Note that nonphysical thicknesses corresponding to values R_B larger than the liquid tin sheet are faded but remain calculable from the thickness model.[20] We observe that the thickness at the inflection point progressively decreases between 0.2 and 0.6 t/τ_c from approximately 120 to 30 nm at which point it appears to level out: no significant change in thickness (at the inflection point) is observed for $t/\tau_c > 0.3$–0.4. We interpret this "converged" thickness, far away from nonphysical interpretation near the sheet edge, as the relevant estimator for h^*.

We next extract the *difference* blocking radius ΔR_B and the corresponding thickness at R_B at a common time $t/\tau_c = 0.3$ for all measured I_{VP}, as presented in Fig. 6 (we refer to Fig. 8 in the Appendix for the underlying heatmaps). We select the delay step 0.3 t/τ_c because it consistently captures both the initial rise and subsequent drop in the PD signal throughout the investigated range I_{VP} (see Fig. 8) although it lies at the limit of the converged thickness range, overestimating h^*.

Figure 6(a) presents ΔR_B as a function of I_{VP} for the selected $t/\tau_c = 0.3$. We observe that for all I_{VP}, ΔR_B exhibits an inflection point t_i that occurs earlier and at larger ΔR_B for higher I_{VP}. We also compute the thickness at R_B for each I_{VP} in Fig. 6(b) following the same procedure as before and find that the thickness of the inflection point h_i decreases with increasing I_{VP}, in line with expectations, cf. Eq. (3). We find closer agreement between the time-resolved approach to obtain h_i (open markers) and the predictions (red line) than in the case of time-integrated plasma emission data cf. Fig. 3(c), filled markers, although the intensity scaling is not in close agreement. This difference in scaling may be due to the fact that, again, Eq. (3) should be interpreted as an upper limit and that the intensity scaling exponent α of t_{on} will differ from the value $\alpha = -2$ (within the range of $-2 < \alpha < -1$). A value of this exponent in this range would bring the observed scaling back into agreement. To avoid dependence on the inferred thickness h_i and the related assumptions and systematic errors, we instead focus on the time of inflection, shown in Fig. 6(d). We attribute an uncertainty of 5% in the measured I_{VP}, which is represented as the x-axis error, and an uncertainty of ± 150 ps in t_i, corresponding to the specified rise time of the photodiode. These data are close to the plasma onset time predicted by Eq. (2), within experimental uncertainty, although again a difference in the scaling exponent may be observed consistent with that of h_i.

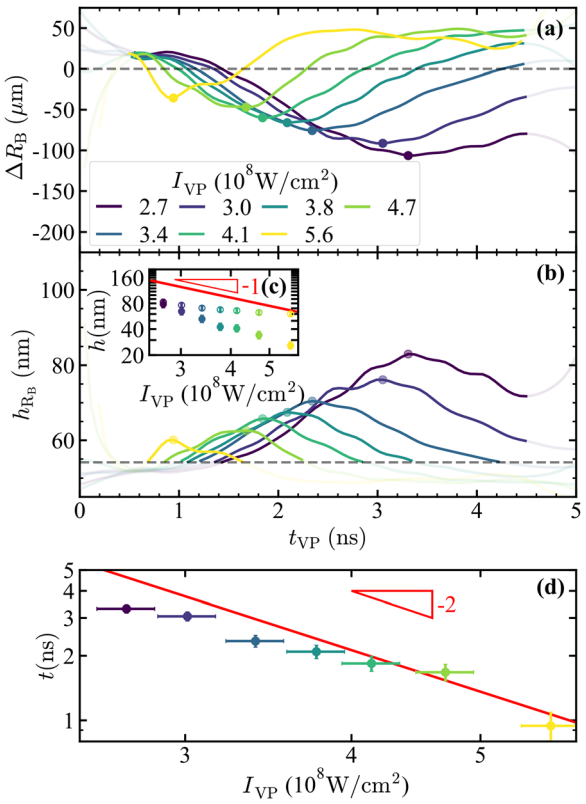

FIG. 6. (a) Difference blocking radius ΔR_B as a function of the VP timescale t_{VP} at $t/\tau_c = 0.3$ for multiple I_{VP}. (b) Sheet thickness h at the blocking radius R_B at $t/\tau_c = 0.3$. Inset (c) thickness at inflection point as a function of I_{VP} (open circles); data from Fig. 3(c) are also shown for comparison (closed circles), and the red line is the threshold thickness h^* cf. Eq. (3). (d) Time of inflection as a function of I_{VP} with the plasma onset time t_{on} cf. Eq. (2).

16 April 2026 10:00:48

© Author(s) 2026

Finally, in Fig. 7 we populate the diagram cf. Fig. 2 with experimental data. The experimental points are extracted by examining the times between 0.2 and 0.4 t/τ_c in the steps of 0.02 t/τ_c. In each time step, we extract the inflection time t_i and threshold thickness h_i, and plot them for all I_{VP} values. The comparison between the experimental data and the theory shows good agreement between the investigated range and times I_{VP}. We observe that at lower I_{VP}, t_i is systematically slightly lower than the theoretical prediction, again in line with the interpretation of Eq. (2) as an upper limit and the fact that its power exponent is expected to differ from -2. Overall, we find reasonable agreement between the model prediction and the time-resolved experimental data, where again no fit was performed and instead fundamental data from previous work (specifically parameters A and B) were combined to predict the threshold behavior in the intermediate case of interfacing bulk and thin film regimes.

IV. CONCLUSION

In this study, we investigate the spatial and temporal dynamics of plasma formation on liquid tin sheets by irradiating them during the droplet deformation process with a 5 ns vaporization laser pulse featuring a spatial and temporal box profile. For intensities around $I_{VP} \sim 10^8$ Wcm^{-2}, we observe plasma formation on sheets during the target deformation process. We employ imaging to detect plasma emission and photodiodes to measure laser pulse transmission past the sheet. The temporally integrated shadowgraphy frames reveal that the extent of the sheet plasma does not continuously follow the liquid tin sheet boundary during deformation. Instead, it corresponds to an intensity-dependent thickness threshold: plasma formation occurs at thicker, more central sheet regions, whereas full local vaporization occurs in thinner, outer regions. Photodiode traces reveal that during the 5 ns VP, the laser transmission exhibits an inflection point, characterized by a distinct decrease in transmission following an initial rise, indicating an intensity-specific onset time within the duration of the VP pulse. We attribute the observed inflection point to the moment when the vapor and plasma phases intersect. We hypothesize that plasma formation on the tin sheet begins at its center, following the bulk plasma onset time $\sim 1/I_{VP}^2$). Subsequently, our interpretation of a single blocking radius indicates that the plasma propagates radially outward. However, experimental limitations (including the strong simplification in assuming a single circular blocking geometry) and uncertainty in accurately determining a unique threshold thickness lead us to mainly keep the focus on the time of inflection. Future work may include time-resolved imaging of plasma light emission to further study the physical origins of the transmission dynamics. Time-resolved imaging the transmitted VP (with a controlled numerical aperture) would possibly enable identifying plasma lensing effects.

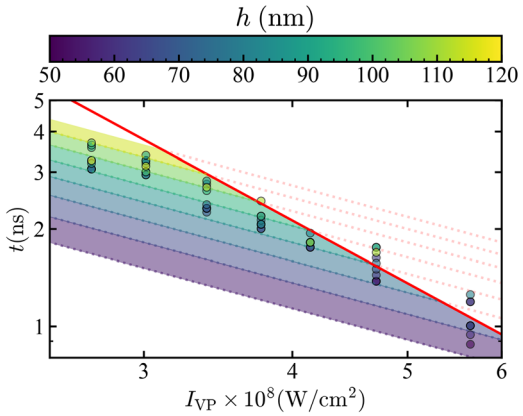

FIG. 7. Zoomed-in view (cf. Fig. 2) and comparison with experimental data on vaporization time, where $t_{VP} \propto I_{VP}^{-1}$ [see Eq. (1)], for various initial thicknesses (indicated by the color bar). The plasma onset time, $t_{on} \propto I_{VP}^{-2}$ [Eq. (2)], is shown in red. Experimental data for the inflection time and corresponding thickness are indicated by markers, with their color representing the inflection thickness as given by the color bar.

Finally, we produce a phase map using all experimental inflection time and thickness data and show reasonable agreement with a model that combines preexisting scaling laws governing vaporization time (which scales as $\sim 1/I_{VP}$) and plasma onset time ($\sim 1/I_{VP}^2$). These findings are particularly relevant for target preparation and metrology in extreme-ultraviolet (EUV) light sources utilizing tin microdroplets.

ACKNOWLEDGMENTS

This work was carried out at the Advanced Research Center for Nanolithography (ARCNL). ARCNL is a public-private partnership with founding partners UvA, VU, NWO-I, and ASML and associate partner UG. This research was funded by the European Research Council (ERC StG 802648). The authors thank Haining Wang and Jorge Gonzalez for valuable discussion, and Henk-Jan Boluijt and Laurens van Buuren for their work on the experimental setup.

AUTHOR DECLARATIONS

Conflict of Interest

The authors have no conflicts to disclose.

Author Contributions

H. K. Schubert: Conceptualization (equal); Data curation (equal); Formal analysis (equal); Investigation (equal); Methodology (equal); Validation (equal); Visualization (equal); Writing – original draft (equal); Writing – review & editing (equal). **R. A. Meijer:** Conceptualization (equal); Data curation (equal); Investigation (equal); Methodology (equal); Supervision (equal); Writing – original draft (equal); Writing – review & editing (equal). **B. Liu:** Conceptualization (equal); Investigation (equal); Writing – review & editing (equal). **D. J. Engels:** Investigation (equal); Writing – review & editing (equal). **O. O. Versolato:** Conceptualization (equal); Funding acquisition (equal); Investigation (equal); Supervision (equal); Writing – review & editing (equal).

DATA AVAILABILITY

The data that support the findings of this study are available from the corresponding author upon reasonable request.

APPENDIX: HEATMAPS OF VP TRANSMISSION FOR VARIOUS VP LASER INTENSITIES

Figure 8 shows the heatmaps of the VP transmission (cf. Fig. 4) for various I_{VP}. These data underlie Figs. 6 and 7 in the main text.

16 April 2026 10:00:48

© Author(s) 2026

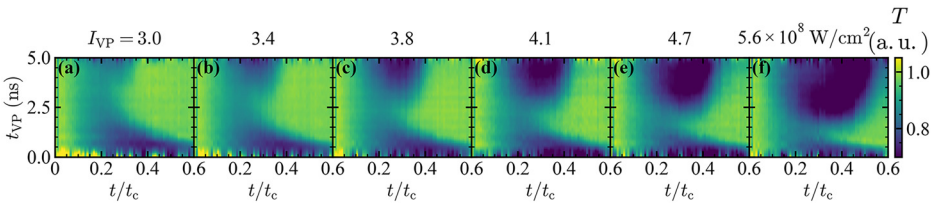

FIG. 8. PD VP transmission heatmaps for multiple I_{VP} (cf. Fig. 4). See the main text.

REFERENCES

[1]H. U. Krebs, M. Weisheit, J. Faupel, E. Süske, T. Scharf, C. Fuhse, M. Störmer, K. Sturm, M. Seibt, H. Kijewski, D. Nelke, E. Panchenko, and M. Buback, Adv. Solid State Phys. **43**, 101 (2003).

[2]S. M. Rossnagel, J. Vac. Sci. Technol. A **21**, S74 (2003).

[3]D. W. Hahn and N. Omenetto, Appl. Spectrosc. **66**, 347 (2012).

[4]L. Yongchao, F. Yao, Z. Yao, S. Yaochun, and S. Yaochun, Photonics **10**, 783 (2023).

[5]S. P. Murzin, Metals **14**, 1458 (2024).

[6]H. Mizoguchi, H. Nakarai, T. Abe, K. M. Nowak, Y. Kawasuji, H. Tanaka, Y. Watanabe, T. Hori, T. Kodama, Y. Shiraishi, T. Yanagida, G. Soumagne, T. Yamada, T. Yamazaki, S. Okazaki, and T. Saitou, Adv. Opt. Technol. **4**, 297 (2015).

[7]I. Fomenkov, D. Brandt, A. Ershov, A. Schafgans, Y. Tao, G. Vaschenko, S. Rokitski, M. Kats, M. Vargas, M. Purvis, R. Rafac, B. La Fontaine, S. De Dea, A. LaForge, J. Stewart, S. Chang, M. Graham, D. Riggs, T. Taylor, M. Abraham, and D. Brown, Adv. Opt. Technol. **6**, 173–186 (2017).

[8]I. Fomenkov, A. Schafgans, and D. Brandt, Synchrotron Radiat. News **32**, 3 (2019).

[9]O. O. Versolato, Plasma Sources Sci. Technol. **28**, 083001 (2019).

[10]D. J. Engels, R. A. Meijer, H. K. Schubert, W. J. van der Zande, W. Ubachs, and O. O. Versolato, Appl. Phys. Lett. **123**, 254102 (2023).

[11]H. K. Schubert, D. J. Engels, R. A. Meijer, B. Liu, and O. O. Versolato, Phys. Rev. Res. **6**, 023182 (2024).

[12]B. Liu, R. A. Meijer, J. Hernandez-Rueda, D. Kurilovich, Z. Mazzotta, S. Witte, and O. O. Versolato, J. Appl. Phys. **129**, 053302 (2021).

[13]D. J. Engels, H. K. Schubert, M. Kharbedia, W. Ubachs, and O. O. Versolato, Phys. Rev. Res. **7**, 023307 (2025).

[14]R. A. Meijer, D. Kurilovich, B. Liu, Z. Mazzotta, J. Hernandez-Rueda, O. O. Versolato, and S. Witte, Appl. Phys. A **128**, 570 (2022).

[15]H. Gelderblom, H. Lhuissier, A. Klein, W. Bouwhuis, D. Lohse, E. Villermaux, and J. Snoeijer, J. Fluid Mech. **794**, 676 (2016).

[16]E. Villermaux and B. Bossa, J. Fluid Mech. **668**, 412 (2011).

[17]A. L. Klein, W. Bouwhuis, C. W. Visser, H. Lhuissier, C. Sun, J. H. Snoeijer, E. Villermaux, D. Lohse, and H. Gelderblom, Phys. Rev. Appl. **3**, 044018 (2015).

[18]D. Kurilovich, A. L. Klein, F. Torretti, A. Lassise, R. Hoekstra, W. Ubachs, H. Gelderblom, and O. O. Versolato, Phys. Rev. Appl. **6**, 014018 (2016).

[19]Y. Wang and L. Bourouiba, J. Fluid Mech. **814**, 510 (2017).

[20]B. Liu, D. Kurilovich, H. Gelderblom, and O. O. Versolato, Phys. Rev. Appl. **13**, 024035 (2020).

[21]B. Liu, R. A. Meijer, W. Li, J. Hernandez-Rueda, H. Gelderblom, and O. O. Versolato, Phys. Rev. Appl. **20**, 014048 (2023).

[22]J. Gonzalez, D. J. Engels, D. J. Hemminga, O. O. Versolato, and J. Sheil, "Formation of a strongly radiative plasma from a Sn vapour due to the presence of nanoparticles" (unpublished).

[23]C. V. Bindhu, S. S. Harilal, M. S. Tillack, F. Najmabadi, and A. C. Gaeris, Appl. Spectrosc. **58**, 719 (2004).

16 April 2026 10:00:48

© Author(s) 2026